PAPER • OPEN ACCESS

Spin detection with a micromechanical trampoline: towards magnetic resonance microscopy harnessing cavity optomechanics

To cite this article: R Fischer *et al* 2019 *New J. Phys.* **21** 043049

View the article online for updates and enhancements.

New Journal of Physics

The open access journal at the forefront of physics

CrossMark

PAPER

Spin detection with a micromechanical trampoline: towards magnetic resonance microscopy harnessing cavity optomechanics

R Fischer[1,2,3], D P McNally[1,2], C Reetz[1,2], G G T Assumpção[1,2], T Knief[1,2], Y Lin[1,2,4] and C A Regal[1,2]

1 JILA, National Institute of Standards and Technology and University of Colorado, Boulder, CO 80309, United States of America
2 Department of Physics, University of Colorado, Boulder, CO 80309, United States of America
3 Rafael Ltd, Haifa 31021, Israel
4 Current address: CAS Key Laboratory of Microscale Magnetic Resonance and Department of Modern Physics, University of Science and Technology of China, Hefei 230026, People's Republic of China.

E-mail: regal@colorado.edu

Abstract

We explore the prospects and benefits of combining the techniques of cavity optomechanics with efforts to image spins using magnetic resonance force microscopy (MRFM). In particular, we focus on a common mechanical resonator used in cavity optomechanics—high-stress stoichiometric silicon nitride (Si_3N_4) membranes. We present experimental work with a 'trampoline' membrane resonator that has a quality factor above 10^6 and an order of magnitude lower mass than a comparable standard membrane resonators. Such high-stress resonators are on a trajectory to reach $0.1 \, aN/\sqrt{Hz}$ force sensitivities at MHz frequencies by using techniques such as soft clamping and phononic-crystal control of acoustic radiation in combination with cryogenic cooling. We present a demonstration of force-detected electron spin resonance of an ensemble at room temperature using the trampoline resonators functionalized with a magnetic grain. We discuss prospects for combining such a resonator with an integrated Fabry–Perot cavity readout at cryogenic temperatures, and provide ideas for future impacts of membrane cavity optomechanical devices on MRFM of nuclear spins.

1. Introduction

The field of cavity optomechanics, in which mechanical motion is well coupled to an optical resonator, has seen rapid progress in recent years, with applications in particular to utilizing and achieving a quantum regime [1]. Experimenters have harnessed unique mechanical resonators with both high resonant frequencies, which favor the observation of quantum effects in comparison to thermal scales, and high quality factors that offer environmental isolation. In particular tensioned elements, for example silicon nitride (Si_3N_4) strings or drums, were found to be well-adapted to cavity optomechanics [2], and ultracoherent mechanical tensioned resonators have been enabled by engineering phononic bandgaps and bending profiles [3–7]. A result of this development is a class of mechanical resonators with novel force sensing prospects, thanks to a combination of high force sensitivity, high resonant frequencies, and compatibility with excellent displacement readout.

In this article, we focus on sensing spins in solids with magnetic resonance force microscopy (MRFM) using a membrane mechanical resonator [8] engineered for high-Q and low mass in a platform compatible with a cavity-optomechanical device. Standard magnetic imaging techniques, utilizing inductive detection schemes, reach sensitivities of 10^{13} nuclear spins or 10^{10} electron spins. MRFM combines ideas of magnetic resonance imaging (MRI) and scanning probe microscopy in a method that has prospects to significantly reduce the number of spins and the corresponding voxel size that can be detected in magnetic imaging [9]. If sensitivity at the single-spin level could be realized, three-dimensional images of molecules such as proteins could be taken at the atomic scale [10–12]. MRFM relies upon extreme force sensitivities that have reached the atto-newton level in experiments to date [13]. This has enabled measurement of a single electron spin [14], or a small ensemble of nuclear spins, corresponding to less than 10nm resolution [15, 16]. Achieving the extreme sensitivities required

Figure 1. Concept of force detected magnetic resonance microscopy with cavity optomechanical coupling. A single mechanical mode is coupled to an optical cavity (red) and to a spin sample (green) at spatially separate locations. The mechanical mode (ω_m) could in principle be resonant with the Larmor frequency of nuclear spins in the sample. A magnet (orange) affixed to the resonator creates a large gradient that provides the magnetic coupling and spatial resolution based on magnetic resonance (orange slice). (Note the spin could alternatively be fixed to the resonator, and correspondingly the magnet to an external tip). An external homogeneous magnetic field B_0 dominates the direction and magnitude of the total magnetic field. (See figure 7 for more detail of bias field and gradient orientations for different detection configurations.)
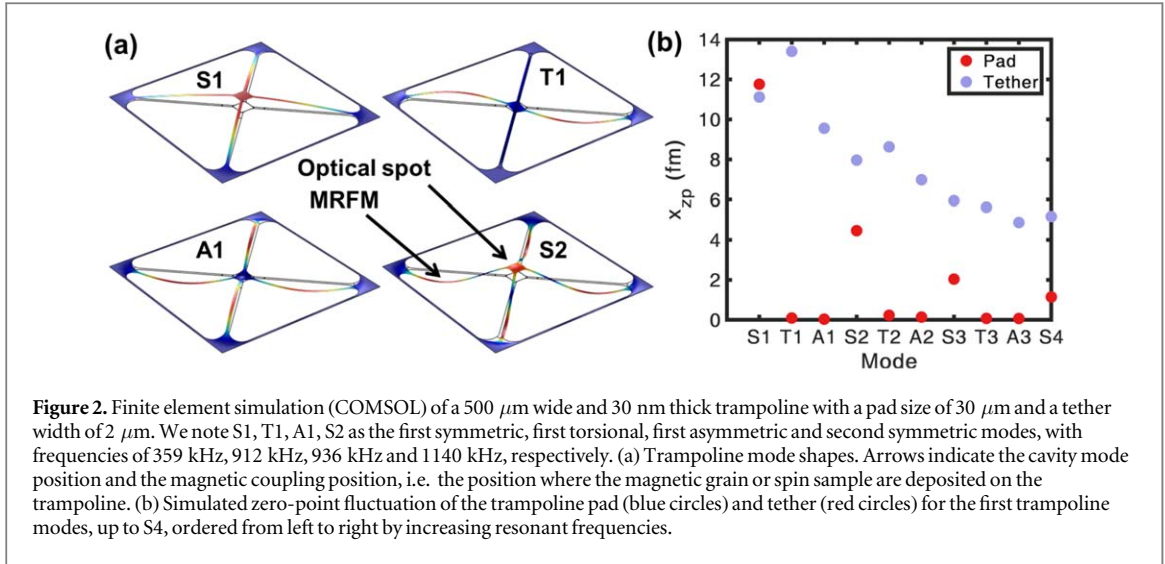
for this demanding imaging technique have been a long-standing challenge [17]. Further, nanoscale magnetometers using nitrogen vacancy (NV) centers in diamond have provided an alternative and rapidly-growing route to nanoscale magnetic imaging [18–25]. However, the challenges of achieving a sensitive force sensor at a nanometric scale are orthogonal to realizing a long coherence NV defect close to the diamond surface [26–29].

We identify a number of distinct benefits of a cavity optomechanics platform for force-detected magnetic resonance. In a future fully-integrated system, we envision a concept as shown in figure 1 in which cavity optomechanical and magnetic coupling are realized simultaneously. Although illustrated with a Fabry–Perot cavity and a silicon nitride (SiN) membrane, the optical integration could take many forms and benefit from a variety of current cavity optomechanics techniques [30–33]. Electromechanical couplings could also be used if they are designed to tolerate the large magnetic fields required for magnetic resonance [34]. Cavity optomechanical damping, analogous to active damping commonly used in force sensing [35], has demonstrated cooling mechanical resonators to their quantum ground state [36–38]. Although this damping does not enhance force sensitivity, deep passive damping using a cavity enables increases in bandwidth combined with an excellent displacement sensitivity.

In the context of mechanical devices, engineered SiN membrane resonators offer the promise of potentially record force sensitivities among devices compatible with cavity optomechanics; we project sensitivities below $0.1 \, \text{aN}/\sqrt{\text{Hz}}$ [3, 5, 6, 39] in a dilution refrigerator environment. Further, these sensitivities can be achieved at higher frequency of operation—at the MHz scale and likely above. Here one expects to reduce $1/f$ noise encountered due to surface effects, which is a limiting factor in MRFM and has been explored in the context of MHz frequency nanowire sensors [40].

If mechanical frequencies of high-force sensitivity resonators can be pushed to 10 MHz and beyond, direct resonant coupling between the nuclear spins and the mechanical resonator can be achieved at Tesla-scale magnetic fields. Most spin-sensing protocols to date rely on the response of a mechanical resonator to a driven magnetization variation. Resonant coupling could enable distinct readout capabilities and potential access to information on transverse magnetization, as achieved via magnetic induction detection of NMR or electron spin resonance (ESR) [8, 41, 42]. Combining strong resonant spin-mechanical coupling with cavity optomechanical coupling to a cold optical bath may enable cooling of the spin ensemble, and corresponding control of the ensemble spin polarization [20, 42–45]. This proposed resonant coupling for nuclear spins would be analogous to recent experiments and proposals utilizing direct resonant coupling between electron spins and 10 GHz scale microwave (MW) cavities [46, 47].

In this article, we present work in which we harness a membrane resonator engineered for low mass and high-Q, known as a trampoline resonator [48–50] for spin detection [51–53]. Square SiN membranes have previously been used for MRFM [8], torque magnetometry [54], and force-detected ESR [55]. Here we follow the work of [8] by studying a significantly lower effective mass resonator, and develop a compact platform that will be conducive to cavity optomechanical integration. First, we demonstrate that trampoline resonators can maintain quality factors above 10^6 after being functionalized with a magnetic grain, and present a general framework for understanding force sensing using complex resonant modes. These complex modes allow effective separation of the optical and the mechanical interaction positions, essential for cavity integration.

Figure 2. Finite element simulation (COMSOL) of a 500 μm wide and 30 nm thick trampoline with a pad size of 30 μm and a tether width of 2 μm. We note S1, T1, A1, S2 as the first symmetric, first torsional, first asymmetric and second symmetric modes, with frequencies of 359 kHz, 912 kHz, 936 kHz and 1140 kHz, respectively. (a) Trampoline mode shapes. Arrows indicate the cavity mode position and the magnetic coupling position, i.e. the position where the magnetic grain or spin sample are deposited on the trampoline. (b) Simulated zero-point fluctuation of the trampoline pad (blue circles) and tether (red circles) for the first trampoline modes, up to S4, ordered from left to right by increasing resonant frequencies.

Second, as an initial spin-sensing demonstration, we detect an ensemble of fast-decaying electron spins of diphenylpicrylhydrazil (DPPH) at room temperature using a moderate magnetic field gradient created with a permanent magnetic grain affixed to the trampoline resonator. The detection scheme here is based on a Michelson interferometer, while an optical cavity integration is left for future work. We conclude with a discussion of the implications of our work for full cavity optomechanical integration of MRFM at cryogenic temperatures, and the detection of nuclear spins.

2. Functionalization of high-tension mechanics

2.1. Concept

Independent of the particular spin-sensing goal, a common thread in force-detected resonance is the effective functionalization of the mechanical element of choice. To harness the high-Q and complex geometries of Si_3N_4 resonators [5], we must (1) learn to place magnets or samples on these resonators with minimal reduction of their quality factor and (2) understand through numerical modeling how mechanical geometry affects both the magnetic coupling and optical coupling as a function of spatial position on the resonator.

In our approach to functionalization, we spatially separate the optical cavity mode and the magnetic coupling achieved by depositing spins or a magnet on the mechanical resonator (figure 2(a)). To describe the associated interaction terms we find it convenient to use quantum scales; however this analysis translates well to the classical limit relevant to our proposed sensing applications. The optomechanical single-photon single-phonon coupling is $g_{0,OM} = \hbar \frac{\omega_{cav}}{L} x_{zp}$ [1], where ω_{cav} and L are the cavity mode frequency, and the cavity length respectively, and x_{zp} is the zero-point fluctuation. On the other hand, the spin-mechanical single-spin single-phonon coupling term (see appendix A) is

$$g_{SM} = \hbar\gamma\frac{\partial B}{\partial x}x_{zp}. \tag{1}$$

Here γ and $\frac{\partial B}{\partial x}$ are the electron or nuclear gyromagnetic ratio and the magnetic gradient, respectively. Both coupling terms above are linear in x_{zp}; however, effectively, the zero-point fluctuation is position and mode dependent, due to the resonator spatial mode shape. The effective mass, m_{eff} that determines the zero-point fluctuation

$$x_{zp} = \sqrt{\frac{\hbar}{2m_{eff}\omega_m}} \tag{2}$$

is a function of the position and the mechanical mode:

$$m_{eff,j}(x, y) = m_{phys}\frac{\int_{S_{tot}} w_j^2(u, v)\,\mathrm{d}u\mathrm{d}v \Big/ \int_{S_{tot}} \mathrm{d}u\mathrm{d}v}{w_j^2(x, y)}, \tag{3}$$
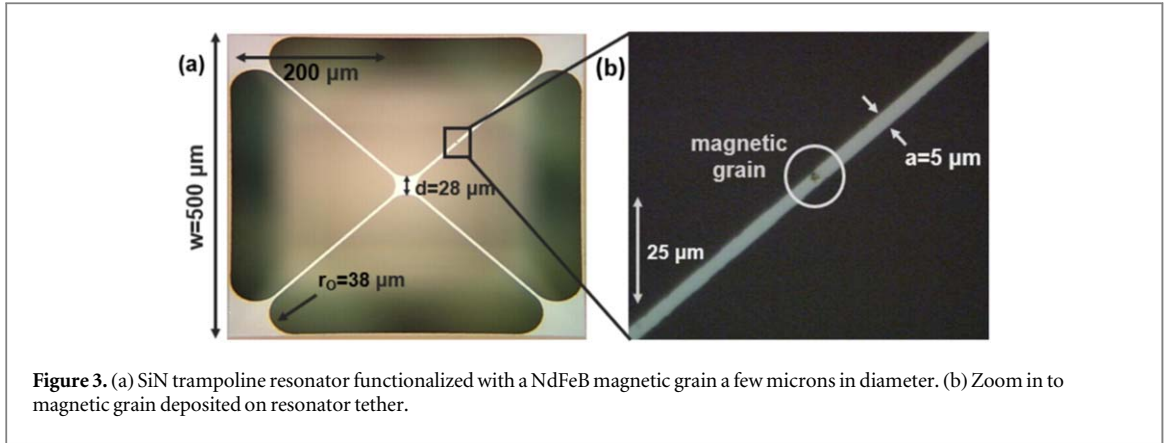
Figure 3. (a) SiN trampoline resonator functionalized with a NdFeB magnetic grain a few microns in diameter. (b) Zoom in to magnetic grain deposited on resonator tether.

Table 1. Critical dimensions of each trampolines in devices A and B. t is the SiN thickness, w is window size, r_o is the outer fillet radius, d the central pad length, a is the tether width, and m_{eff} is the calculated resonator's effective mass of the fundamental mode, at the pad position, using equation (3). Dimensions are depicted in figure 3.

Device	A	B
t	30 nm	70 nm
w	500 μm	500 μm
r_o	36 μm	15 μm
d	28 μm	28 μm
a	5 μm	5 μm
m_{eff}	0.5 ng	0.9 ng

where m_{phys} is the physical mass of the resonator, and w_j is the j-mode shape along the x-axis, S_{tot} is the total surface of the trampoline. Therefore, positioning the optical cavity mode and the magnetic grain at different locations allows optimization of the physical couplings. As an example in figure 2(b), we show a simulation of x_{zp} of several modes of trampoline, with a fundamental mode frequency of 359 kHz. x_{zp} is calculated separately for the pad and the tether using equations (2), (3). We see that, for a given trampoline design, only the symmetric modes allow simultaneous opto-mechanical and spin-mechanical interaction. Moreover, the optimal MRFM detection position will depend both on the trampoline mode, as well as on the deposited sample. Specifically, the sensitivity of magnetic force detection scheme is determined by the thermal vibration level of the resonator. The force noise power spectrum is given by the fluctuation–dissipation theorem:

$$S_F = \frac{4k_B T k}{\omega_m Q} = \frac{2\hbar k_B T}{Q x_{zp}^2},$$

(4)

where k is the resonator spring constant, Q is the quality factor, ω_m is the mechanical angular frequency. Therefore, to maximize force sensitivity, both the resonator's Q, along with its x_{zp} should be maximized.

2.2. Mechanical design and characterization of magnet-deposited membranes

We now present our experimental work on magnetic functionalization of trampoline resonators. We use the 4-tether trampoline design of [49], with the geometric parameters depicted in figure 3, and detailed in table 1, for two mechanical devices, marked A and B. The trampolines were deposited with an NdFeB magnetic grain with dimensions of a 2–3 μm, to generate magnetic coupling between the trampoline and the spin sample. The grain was deposited on one of the tethers ~100 μm from the pad. Further details on the deposition procedure and the trampoline fabrication appear in appendices C and D, respectively.

The frequency and Q of the mechanical resonators, before and after assembly, were measured by an optical setup based on a Michelson interferometer [56]. The resonators were mounted inside a vacuum chamber with a pressure of ~10^{-6} Torr. The interferometer signal beam was focused onto the trampoline pad with a spot size of 30 μm. The mechanical resonant frequencies were identified within the device's thermal spectrum, while the quality factors were measured by resonantly exciting the modes by a ring piezoelectric actuator. The excitation is abruptly stopped and the energy decay time τ_m is extracted, where $Q = \omega_m \tau_m$. Resonant frequencies and Q of two resonator chips before and after deposition appear in table 2. There, we see that although the epoxy and the magnetic grain are mechanically lossy, the small amount deposited still allow Qs above 10^6, while slightly
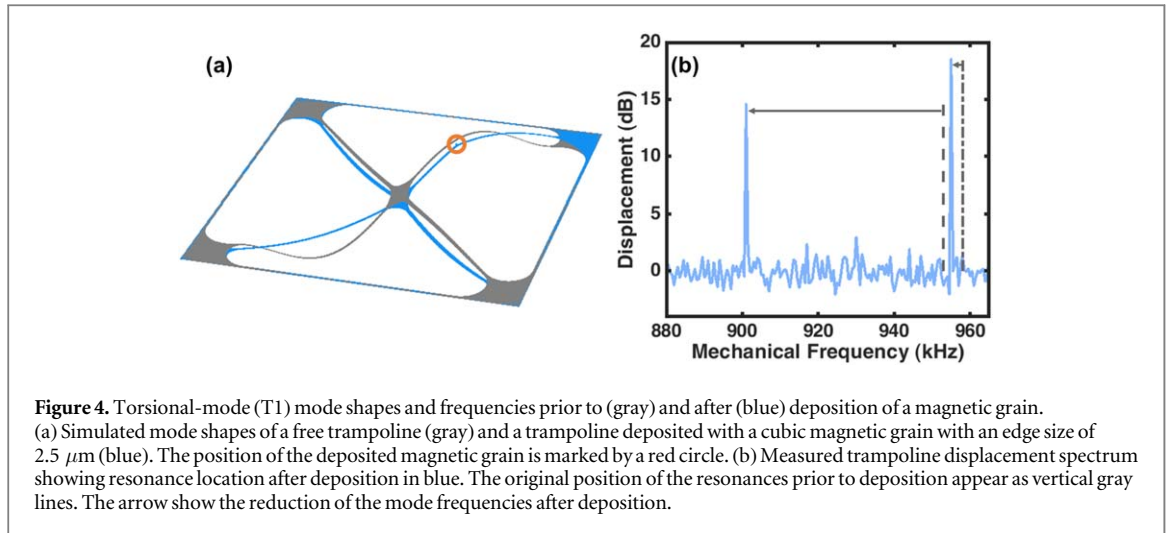
Figure 4. Torsional-mode (T1) mode shapes and frequencies prior to (gray) and after (blue) deposition of a magnetic grain. (a) Simulated mode shapes of a free trampoline (gray) and a trampoline deposited with a cubic magnetic grain with an edge size of 2.5 μm (blue). The position of the deposited magnetic grain is marked by a red circle. (b) Measured trampoline displacement spectrum showing resonance location after deposition in blue. The original position of the resonances prior to deposition appear as vertical gray lines. The arrow show the reduction of the mode frequencies after deposition.

Table 2. Fundamental mode frequencies and quality factors of the resonators before and after deposition of the NdFeB magnetic grain, calculated spring constant and zero-point fluctuation (derived from the effective mass of table 1), and the corresponding room-temperature force sensitivity, after deposition.

	Device	A	B
Trampoline	f_{S1}	429.1 kHz	389.8 kHz
	Q	4.5×10^6	1.8×10^6
Trampoline with magnet	f_{S1}	413.2 kHz	379.6 kHz
	Q	2.4×10^6	1.7×10^6
	k	3.4 N m^{-1}	5.3 N m^{-1}
	x_{zp}	6.3 fm	4.9 fm
	$\sqrt{S_F}$	67 aN/$\sqrt{\text{Hz}}$	102 aN/$\sqrt{\text{Hz}}$

reducing the resonance frequency. This optical setup was used for the magnetic force detection in this article as well, as described in the next section.

After the magnetic grain is deposited, successful grain retention can be verified by the large frequency shift of one of the torsional T1 modes. For a perfectly symmetric bare trampoline, there are two degenerate T1 modes, representing the torsion of one pair of opposing tethers about the other perpendicular pair (figure 2(a)). For Device A, the bare trampoline's slight asymmetry resulted in a few kHz shift between the two T1 modes (figure 4 —gray). After deposition, however, the symmetry between the tethers is broken, and the frequency of the torsional mode associated with deposited grain decreases significantly, due to the added mass (figure 4—blue). This sensitivity to the presence of the grain can assist in estimating the mass of the deposited grain, as well as clearly indicating the integrity of the mechanical part.

3. Electron-spin detection

3.1. Physical components
The apparatus we use for electron spin detection of DPPH is schematically depicted in figure 5. It is based on a two-chip design, which is comprised of a mechanical resonator chip deposited with a magnetic grain for magnetic gradient application, and sapphire chip with a deposited spin sample and a stripline for MWs excitation of the spin resonance. The two chips are brought in close proximity to one another to enhance the magnetic force between the chips. A macroscopic permanent magnet sets the Larmor frequency of the spins. The displacement of the mechanical resonators is monitored by an optical Michelson interferometer. The two-chips and the magnets are placed in a vacuum chamber at room temperature and pumped to a vacuum level below 10^{-6} Torr, to avoid gas damping of the mechanical resonator.
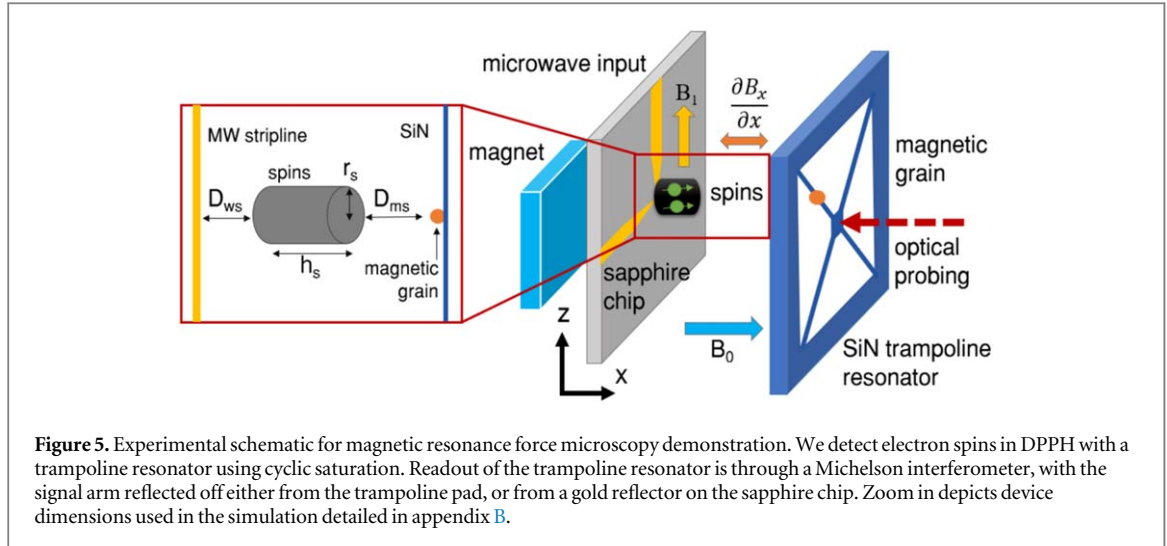
Figure 5. Experimental schematic for magnetic resonance force microscopy demonstration. We detect electron spins in DPPH with a trampoline resonator using cyclic saturation. Readout of the trampoline resonator is through a Michelson interferometer, with the signal arm reflected off either from the trampoline pad, or from a gold reflector on the sapphire chip. Zoom in depicts device dimensions used in the simulation detailed in appendix B.

3.2. Magnetic design

To create the bias field B_0 we use a NdFeB permanent magnet with dimensions of $\frac{1}{2}'' \times \frac{1}{2}'' \times \frac{1}{8}''$ that sets a $B_0 \sim 1000$ G magnetic field on the x-axis, parallel to the vibration direction of the mechanical resonator. B_0 is the dominant field that determines the spins' Larmor frequency $\omega_0 = \gamma_e B_0$, where $\gamma_e = 2.8/(2\pi)$ MHz G^{-1} for electronic spins.

A magnetic grain of NdFeB, with a few μm in dimensions was used for setting the magnetic gradient. The grain was magnetized with an electromagnet along the x-axis, and sets a gradient $\partial B_x / \partial x$. This gradient creates a force between the grain and the spins, equal to $F_x = M_x \cdot \partial B_x / \partial x$, where M_x is the spin sample magnetization along the x-axis. The gradient along the x-axis is determined by the magnetic grain magnetization, size and shape, and its distance from the spin sample. The gradient along the magnetization axis of a spherical magnetic grain with remanent magnetization of B_r, radius of R_M is

$$M_g = -\frac{2R_M^3 B_r}{r^4}, \tag{5}$$

where $r > R_M$ is the distance from the center of the grain. Typical dimensions for our setup included a grain with diameter of 2 μm, at a distance of 10–20 μm, and remanent magnetization of 7 kG, which translates to a gradient between 0.1 and 1 G μm^{-1}. We note that the magnetization was calibrated by a magnetic property measurement system machine using 10 mg of magnetized NdFeB powder.

3.3. Electronic spins

We utilize a DPPH spin sample of 20–30 μm in size. DPPH is used due to its high spin concentration of $\rho_{\text{spin}} \approx 2.1 \times 10^{21}$ spins cm^{-3} and short relaxation time, of 25–80 ns, depending on the sample origin [57–59]. The DPPH thermal magnetization is $M_0 = \frac{\chi_0 B_0}{\mu_0}$, where $\chi_0 = 2.5 \times 10^{-5}$ is the DPPH magnetic susceptibility [60], μ_0 is the vacuum permeability, and B_0 is the magnetic field. For relatively low magnetic gradients of 0.1–1 G μm^{-1} over the DPPH grain, we can estimate the number of spins contributing to the force by simply $V_{\text{DPPH}} \cdot \rho_{\text{spin}} \approx 10^{13}$.

3.4. MW application

A gold stripline deposited on a sapphire substrate delivers a MW tone that drives spin manipulation, as seen in figure C1. A sapphire substrate is chosen due to its relatively high thermal conductivity and high electrical resistivity. The stripline is designed as a 90° corner for application of the MW field, with $B_1 \ll B_0$, perpendicular to B_0 in the y–z plane. The narrowest section of the corner reaches ~20 μm, on the same order of the DPPH grain. The MW is generated by a signal generator and a 3 W amplifier. For 5 mA of current ($\approx$1 mW), we estimate $B_1 \approx 0.5$ G $\Rightarrow \Omega_{\text{Rabi}} \approx 2\pi \times 1.5$ MHz. However, experimental results suggest high loss in the MW delivery, resulting in $B_1 \approx 50$ mG. More details can be found in appendix B.

3.5. MRFM detection

We use an MRFM detection technique known as cyclic saturation [8, 61, 62]. This detection method is appropriate if the spin relaxation time is much shorter than the resonator's period $\tau \ll T = \frac{2\pi}{\omega_m}$. In this case, if a MW tone is modulated at a frequency resonant with one of the mechanical modes the steady-state spin

magnetization can be expressed, according to the Bloch equations [61]. We assume $\tau = T_1 = T_2$, which is typical for DPPH [8, 57]:

$$M_x = M_0\left[1 - \frac{\gamma^2 B_1^2 \tau^2}{1 + (\gamma B_0 - \omega_{\mathrm{MW}})^2 \tau^2 + \gamma^2 B_1^2 \tau^2}\right], \qquad (6)$$

where ω_{MW} is the MW angular frequency, and B_1 and B_0 are the position dependent RF and DC magnetic fields respectively. We utilize two types of cyclic saturation schemes—amplitude modulation (AM), where the amplitude of B_1 is modulated $A_m(t) = A_0 \cdot (1 + m \cdot \sin(\omega_m t))$, and frequency modulation (FM), where its frequency is modulated $\omega_{\mathrm{MW}}(t) = \omega_0 + \omega_{\mathrm{FM}} \cdot \sin(\omega_m t)$, with ω_{FM} the frequency deviation. To calculate the magnetic force applied on the resonator we integrate over the magnetic field distribution, assuming radial symmetry with a magnetic grain magnetized along the symmetry axis:

$$F = 2\pi \int_{x_{\min}}^{x_{\max}} \int_0^{r_{\max}(x)} M_1(x, r) \cdot r \cdot \left.\frac{\partial B_x}{\partial x}\right|_{x,r} \mathrm{d}r\mathrm{d}x, \qquad (7)$$

where $x_{\min} - x_{\max}$, $r_{\max}(x)$ are the DPPH grain boundaries on the x-axis and r-axis, respectively. M_1 is the Fourier component of the modulation at an angular frequency of ω_m. In the case of AM (full modulation) $M_{1,\mathrm{AM}} = \frac{2}{\pi}(M_0 - M_x)$, and for FM $M_{1,\mathrm{FM}} = \omega_{\mathrm{FM}} \cdot \frac{\partial M_x}{\partial \omega_{\mathrm{MW}}}$ [61]. We note here that detection based on FM is more robust versus electrical spurious forces compared to AM, and therefore the main results in section 3.6 are measured in FM.

We use two methods to sweep over the magnetic resonance. The first is varying the MW frequency with a fixed magnetic field, and the second is fixing the MW frequency while varying B_0. To sweep B_0 we add a second NdFeB magnet with dimensions of $2'' \times 1'' \times \frac{1}{2}''$ outside the vacuum chamber, and varied the field between 25 and 43 G, with an opposite magnetization to the first magnet. These fields correspond to a distance of 87 to 75 mm from the flip-chip. The second magnet was added to enable fine scan of B_0, with a mm-resolution displacement, outside of the vacuum chamber.

A complication in the detection is a slow drift of the resonator's frequency. The undamped trampoline resonators used here had a linewidth of ~0.2 Hz, with a few Hz drifts at time scales of a tens of seconds. Future experiments will use passive damping provided by a cavity, but for these initial experiments we simply avoid this drift by sweeping over the mechanical resonance with a range of 10–30 Hz. We verified that the driven amplitude reaches its steady-state value, when increasing the sweep duration. As noted in the discussion section, damping of the resonator would reduce or eliminate the impact of the drifts for coherent detection performance as well as for the efficiency of the acquisition sequence.

3.6. MRFM results and analysis

Figure 6(a) shows a MW frequency sweep of device A, with FM cyclic saturation. The sweep parameters are $\omega_{\mathrm{FM}} = 2\pi \times 10$ MHz, $B_1 \approx 50$ mG. A sweep of the B_0 magnitude with FM cyclic saturation of device B appear in figure 6(b). There, the MW frequency was $\omega_{\mathrm{MW}} = 2\pi \times 2.564$ GHz, and $B_1 \approx 100$ mG with modulation deviation of $\omega_{\mathrm{FM}} = 2\pi \times 10$ MHz. The displacement amplitude was calculated either from the calibrated Michelson setup (figure 6(a)) (device A) or by comparing the displacement enhancement over the estimated thermal signal (figures 6(b), (c)) (device B). For a calibrated Michelson interferometer $A = V_p \cdot C$, where C is the Michelson calibration factor in V nm^{-1}, and V_p is the Michelson amplitude in volts at the mechanical resonance frequency. By measuring the enhancement E over the thermal signal $x_{\mathrm{th}} = \sqrt{k_B T / k}$, we extract the signal amplitude of $A = x_{\mathrm{th}} \cdot E$. To estimate the applied force we calculate the trampoline response to a steady-state resonant excitation as $F = (A \cdot k)/Q$. The conversion factor of k/Q was different between the two chips, as seen in table 2. We note that in all of the measurements only the signal amplitude was acquired (blue), and a sign change was added to the FM force analysis to accommodate the expected phase flip of the FM resonance (red dashed). To estimate the geometric and physical parameters of the flip-chip, a fit to the 2D-magnetic force model, using equation (7), was performed, as seen in figure 6(a) and in figure 6(b). From the fit we derive the flip-chip parameters as appear in table 3. We note that the parameter values were within the estimated range. More details of the MRFM fitting procedure for derivation of the values in table 3 appear in appendix B.

The main limitation for increasing B_1 was the electric spurious force between the two chips. Spurious forces are typical for MRFM setups. However, with this initial flip-chip design we did not apply the various methods intended for coping with electric spurious forces, such as those described in [8, 40, 63, 64]. Unlike the magnetic force, the spurious force is broadband yet structured, and therefore interferes with the magnetic resonance, and at high MW powers overwhelms it. The spurious force is generally more apparent in AM spectra, as we see in (figure 6(c)). In future design and experimental sequence one must consider mitigation of the spurious force to allow more efficient resonant magnetic drive.
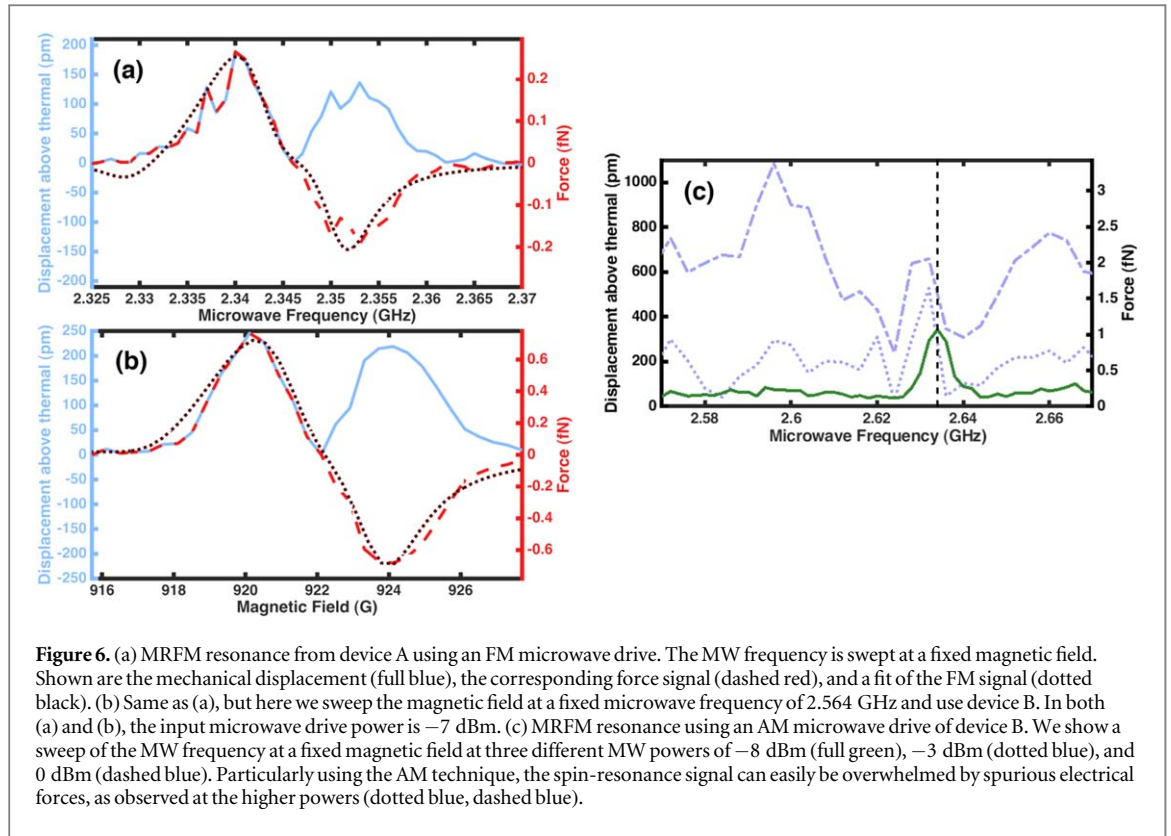
Figure 6. (a) MRFM resonance from device A using an FM microwave drive. The MW frequency is swept at a fixed magnetic field. Shown are the mechanical displacement (full blue), the corresponding force signal (dashed red), and a fit of the FM signal (dotted black). (b) Same as (a), but here we sweep the magnetic field at a fixed microwave frequency of 2.564 GHz and use device B. In both (a) and (b), the input microwave drive power is −7 dBm. (c) MRFM resonance using an AM microwave drive of device B. We show a sweep of the MW frequency at a fixed magnetic field at three different MW powers of −8 dBm (full green), −3 dBm (dotted blue), and 0 dBm (dashed blue). Particularly using the AM technique, the spin-resonance signal can easily be overwhelmed by spurious electrical forces, as observed at the higher powers (dotted blue, dashed blue).

Table 3. Critical dimensions of each flip chip were first estimated from optical microscopy and finite element simulations. Further refinements were determined by fitting data to the model provided by equation (7). r_m is the radius of the magnetic grain, D_{ms} is the distance between magnetic grain and spin ensemble, D_{sw} is the distance between spin grain and MW stripline, r_s is the radius of spin ensemble (cylinder), h_s is the height of spin ensemble (cylinder) B_1 is the MW-frequency magnetic field, τ is the relaxation time of spins, B_0 is the uniform magnetic field, and $\frac{\delta B_0}{\delta x}$ is the local gradient of uniform magnetic field.

Device	A	B
r_m	1.5 μm	1.45 μm
D_{ms}	5 μm	8 μm
D_{sw}	5 μm	5 μm
r_s	15 μm	15 μm
h_s	35 μm	25 μm
B_1	50 mG	80 mG
τ	42 ns	42 ns
B_0	915.7 G	873.8 G
$\delta B_0/\delta x$	20 G mm^{-1}	25 G mm^{-1}

4. Discussion

In the experiments above we laid the groundwork for an integrated platform that couples spins to engineered membrane resonators. We now discuss the prospect for bringing together state-of-the-art tensioned mechanics, magnetic couplings, and high-finesse cavities, as schematically depicted in figure 1.

4.1. Cavity and mechanical integration
Efficient damping is a key component of high-bandwidth spin detection [65]. In our initial work we simply used an undamped trampoline resonator; however, the relaxation time of a high-Q resonator with frequencies of 1–10 MHz can exceed seconds, and even minutes, which is prohibitive to detection protocols. Optical damping facilitated by a high finesse cavity via optomechanical interaction provides a natural method that incorporates high displacement sensitivity and that does not require high-frequency feedback loops (figure 1) [1, 40].

Fabry–Perot cavities with finesse of a few thousand are routinely integrated with membrane resonators [32, 38, 66, 67], and damping rates upward of 10 kHz have been demonstrated in a cryogenic environment down to 100 mK [38]. Note that resonator designs with $x_{zp} \sim 10$ fm, and $\omega_m \leqslant 2\pi \times 10$ MHz imply structures of $\sim 10 \ \mu$m in size. Hence, experiments may require cavities with small mode sizes, which can be achieved with fiber cavities [68] or integrated silicon mirrors [69]. Integrated photonic crystals cavities or whispering gallery mode cavities in conjunction with a variety of high-sensitivity mechanical resonators offer additional prospects [30, 70].

Further, future prospects of this platform will require increasing mechanical quality factors from the 10^6 level demonstrated here, to the 10^8 level required for projected numbers, while achieving both optical and magnetic integration. In this article, we demonstrated that when depositing a micron-size grain on a trampoline tether, a $Q > 10^6$ could be maintained, along with x_{zp} of 5–7 fm. To utilize even higher Q devices of 10^8 or higher [5, 6], a sample (either a magnetic grain or a spin sample, as in figure 1) with smaller dimensions should be deposited. We expect that deposition of magnetic sample with dimensions of less than a micron will require a more integrated deposition method.

4.2. Magnetic resonance

The strength of the magnetic gradient determines the magnetic force magnitude ($F = \hbar \gamma G$, for a single spin) as well as the coherent coupling strength g_{SM}. Both are crucial for increasing spin sensitivity and resolution, and note that ideas such as spin cooling through mechanics requires extreme couplings. In this work, we demonstrated moderate gradients of up to 1 G μm^{-1}, whereas record gradients reached 60 G nm^{-1} [71], almost 5 orders of magnitude stronger. The main challenge in designing a force sensor based on stressed membranes or doubly-clamped strings is the ability to create a separation of tens of nm between the gradient source and the spins that will allow gradients above 10 G nm^{-1}. One can envision a scanning stiff pillar with a gradient source at its end, as depicted in figure 1 that will allow relative position scanning at distances of 100 nm or below.
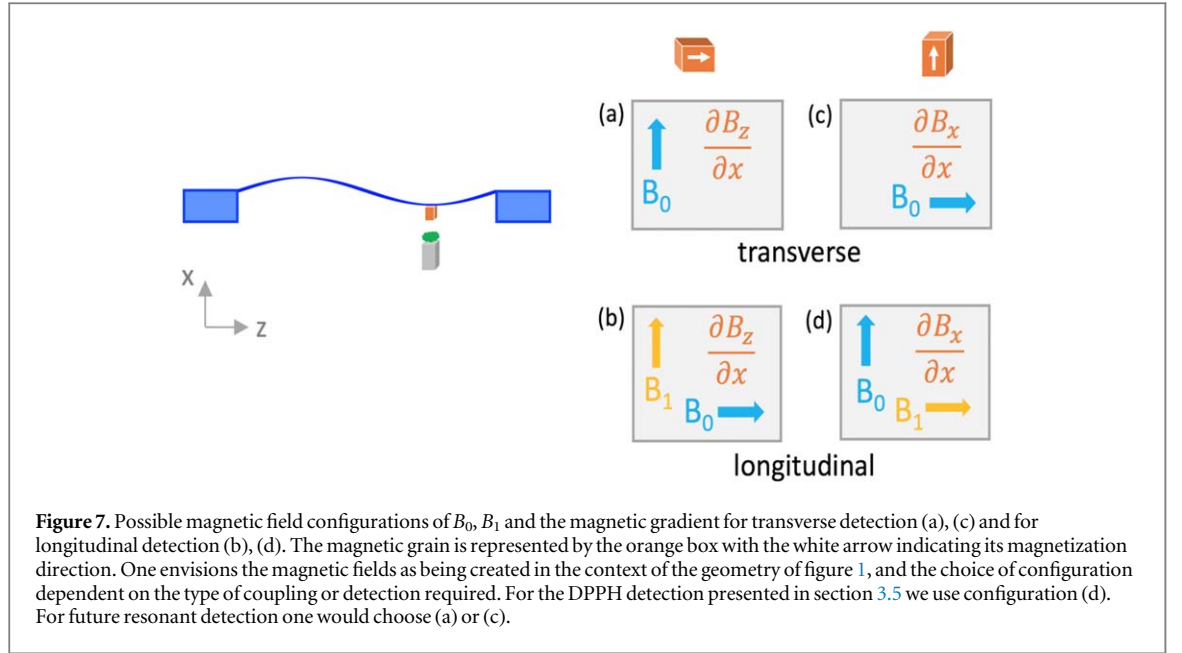
Application of a strong enough B_1 that will allow rapid manipulation of the spins is also an essential component for most MRFM applications. The flip-chip design applied here, with MW application by a non-resonant stripline, achieved only limited B_1 values, below 0.2 G. The stripline design, common in MRFM, is usually integrated with the magnetic gradient source as well [15, 40]. The inherent 2D geometry of tensioned resonator limits stripline designs and a different approach such as a resonant MW circuit [8] should be explored.

Lastly, we review some considerations for spin-mechanics resonant coupling, i.e. operating in a domain where the mechanical resonance and the spin Larmor frequency are matched; MRI experiments have to-date operated with cantilevers with resonant frequencies much smaller than spin frequencies. The associated Larmor frequencies for fields above 3000 G are greater than 10 GHz for electron spins and greater than 10 MHz for nuclear spins. This implies that tensioned SiN devices are suitable for resonant coupling with nuclear spins. (Resonant coupling with electrons could potentially be achieved with silicon optomechanical crystal resonators [36, 72], and has been achieved with MW electromagnetic resonators [46].)

Any detection scheme harnessing resonant detection will be inherently different than standard longitudinal MRFM detection. Because the mechanical and the Larmor frequencies are equal, manipulating the spins at that rate would require strong B_1 fields, as well as breaking the rotating wave approximation. This would make the spin control very challenging. Therefore, two detection schemes can be considered. The first is detecting the spins by starting with a $\pi/2$ pulse followed by Larmor precession that would resonantly drive the spin oscillator. The second is detecting the normal mode splitting or broadening due to strong coupling between the two quantum systems. Both detection schemes require a magnetic gradient of the perpendicular field, as shown in geometries (a), (c) in figure 7. Meaning, for $B_0 \hat{x}$, the gradient would be along $\frac{\partial B_z}{\partial x}$. This is unlike the parallel gradient direction of the standard MRFM, aimed at detection of longitudinal magnetization, which appear in realizations (b), (d) in figure 7.

5. Conclusion

In this work we explored multiple facets of using engineered SiN tensioned membranes for magnetic force sensing. We separated the optical and magnetic interaction positions by depositing a magnetic grain on the trampoline tether and optically measuring the central pad. We integrated these resonators in a flip-chip design and sensed an ensemble of electronic DPPH spins at a force level of 0.1 fN, which improves force sensitivity by almost 2 orders of magnitude over previous spin sensing with tensioned resonators [8]. Our explorations will instruct future integration with a high-finesse cavity for implementation of optomechanical concepts. We discussed future prospects for using tensioned membrane resonators for resonant interaction with nuclear spins, where we envision a major challenge is achieving gradients above 10 G nm^{-1} with planar tensioned resonators.

Figure 7. Possible magnetic field configurations of B_0, B_1 and the magnetic gradient for transverse detection (a), (c) and for longitudinal detection (b), (d). The magnetic grain is represented by the orange box with the white arrow indicating its magnetization direction. One envisions the magnetic fields as being created in the context of the geometry of figure 1, and the choice of configuration dependent on the type of coupling or detection required. For the DPPH detection presented in section 3.5 we use configuration (d). For future resonant detection one would choose (a) or (c).

Acknowledgments

Appendix A. Spin-mechanics Hamiltonian

The force between a magnetic moment $\vec{\mu}$ and a gradient source $\frac{\partial \vec{B}}{\partial x}$ on a mechanical resonator vibrating on the x-axis (figure 7) is $F_x = \vec{\mu} \cdot \frac{\partial \vec{B}}{\partial x}$. For a single spin (either for electronic or nuclear spin) $\vec{\mu} = \mu_{B,N} \cdot \vec{S}$. Then, the spin-mechanics Hamiltonian can be formulated as $H_{SM} = gF_x \cdot x$, where g is the spin g-factor. We express $\vec{S}$ and $x = x_{zp} \cdot (b + b^\dagger)$ as operators, where $b^\dagger$, b are the phonon-states raising and lowering operators, and formally derive

$$H_{SM} = \hbar\gamma x_{zp}(b + b^\dagger)\frac{\partial \vec{B}}{\partial x} \cdot \vec{S}, \tag{A.1}$$

where $\gamma = g\mu_{B,N}/\hbar$ is the gyromagnetic ratio. Therefore, we derive the coupling term of equation (1) as the pre-factor of H_{SM}, in the presence of a magnetic gradient $\frac{\partial \vec{B}}{\partial x}$ as $g_{SM} = \hbar\gamma x_{zp}\frac{\partial \vec{B}}{\partial x}$.

Appendix B. MRFM signal analysis

Fits to the FM modulated cyclic-saturation signals were achieved by numerically calculating equation (7) with $M_1(x, r) = \omega_{FM} \cdot \frac{\partial M_x}{\partial \omega_{MW}}$. Initial parameter values were determined from estimated and literature values and were varied within reasonable uncertainties until a qualitative correspondence between the simulated and measured lineshape was reached. The lineshape of the MRFM signal has a strong dependence on the device geometry outlined in figure 5. The spatial extent of the spin sample gives rise to an inhomogeneous lineshape determined by spatial dependence of B_1, B_0, and $\frac{\partial B_x}{\partial x}$ given by (notations are according to table 3):

$$B_1(x) = \frac{\mu_0 I}{2\pi(h_s - x + D_{sw})} \tag{B.1}$$

$$\vec{B}_0(x, r) = \vec{B}_m(x, r) + \vec{B}_{\text{dip}}(x, r) \tag{B.2}$$

$$\vec{B}_m(x, r) = \left(B_0 + \frac{\delta B_0}{\delta x} x \right) \hat{x} \tag{B.3}$$

$$\frac{\partial B_x}{\partial x}(x, r) = \frac{\partial (B_{\text{dip}})_x}{\partial x} \Bigg|_{x,r}, \tag{B.4}$$

where $\vec{B}_{\text{dip}}(x, r)$ is a magnetic dipole field originating from the center of a spherical magnetic grain with remnant magnetization B_r (equation (5)), and $\vec{B}_m(x, r)$ is the field from the large permanent magnet illustrated in light blue in figure 5. The integration region of the spin is taken to be a cylinder such that $r_{\text{max}}(x) = r_s$. The B_1 field is modeled as the field from a thin wire elbow carrying a current I. B_0 determines the Larmor frequency of the magnetic resonance, while $\frac{\delta B_0}{\delta x}$ corresponds to the spatial gradient of magnetic field from the large permanent magnetic. This gradient is extracted from a finite element simulation (COMSOL) of the large magnet. The fits for the observed MRFM signals indicate that the observed B_1 is significantly weaker than the calculated field from the expected MW transmission; this is consistent with 20 dB loss in the MW line after the MW amplifier.

Appendix C. Flip-chip assembly

The flip-chip device is assembled in three steps: First, the magnetic grain and the DPPH grain are deposited on the resonator and sapphire chips, respectively. Both grains are attached using G1 epoxy from Gatan Inc. Glass tips are used for epoxy and grain deposition, and are maneuvered with a three-axis micropositioner. Second, after the epoxy has cured, the resonator chip is placed between the poles of an electromagnet to magnetize the NdFeB magnetic grain. Third, the two chips are positioned opposite to one another at a distance of 1–10 μm between them, and secured with stycast epoxy, deposited with a glass tip. The sapphire bottom chip of device B has a gold reflector opposite to the trampoline pad to enhance the optical reflection, while device A has a clear optical path for no reflection.
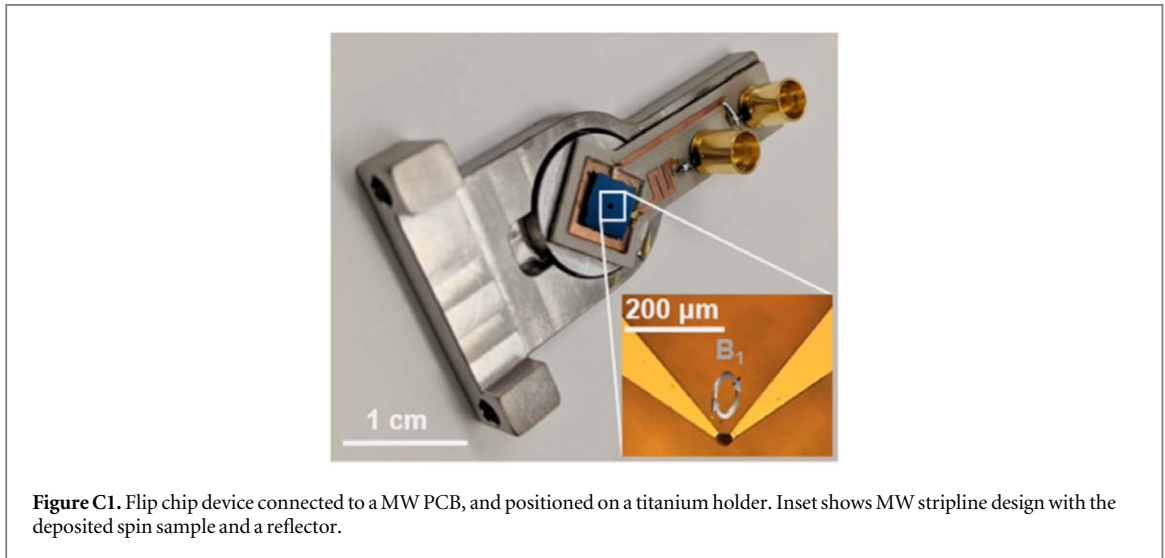

Figure C1. Flip chip device connected to a MW PCB, and positioned on a titanium holder. Inset shows MW stripline design with the deposited spin sample and a reflector.

Appendix D. Trampoline fabrication

Resonators are fabricated from a stoichiometric silicon-nitride (Si_3N_4) clad (80 or 40 nm) silicon wafer (385 μm). The wafer is diced into 5 mm square chips and patterned on both sides. The resonator is written into a PMMA photoresist using a scanning electron microscope. The opposite side of the chip is patterned with a positive UV resist. The exposed Si_3N_4 is etched with a sulfur-hexaflouride reactive ion etch; the silicon is then etched from both sides in a 30% KOH solution for 3.5 hours to release the trampoline. The chip is then cleaned in Nanostrip.

References

[1] Aspelmeyer M, Kippenberg T J and Marquardt F 2014 *Rev. Mod. Phys.* **86** 1391–452
[2] Unterreithmeier Q P, Faust T and Kotthaus J P 2010 *Phys. Rev. Lett.* **105** 027205
[3] Yu P L, Cicak K, Kampel N, Tsaturyan Y, Purdy T, Simmonds R and Regal C 2014 *Appl. Phys. Lett.* **104** 023510
[4] Tsaturyan Y, Barg A, Simonsen A, Villanueva L G, Schmid S, Schliesser A and Polzik E S 2014 *Opt. Express* **22** 6810–21
[5] Tsaturyan Y, Barg A, Polzik E S and Schliesser A 2017 *Nat. Nanotechnol.* **12** 776
[6] Ghadimi A H, Fedorov S A, Engelsen N J, Bereyhi M J, Schilling R, Wilson D J and Kippenberg T J 2018 *Science* **360** 764–8
[7] Teufel J D, Li D, Allman M S, Cicak K, Sirois A J, Whittaker J D and Simmonds R W 2011 *Nature* **471** 204–8
[8] Scozzaro N, Ruchotzke W, Belding A, Cardellino J, Blomberg E C, McCullian B A, Bhallamudi V P, Pelekhov D V and Hammel P C 2016 *J. Magn. Reson.* **271** 15–20
[9] Sidles J A, Garbini J L, Bruland K, Rugar D, Züger O, Hoen S and Yannoni C 1995 *Rev. Mod. Phys.* **67** 249
[10] Sushkov A O, Lovchinsky I, Chisholm N, Walsworth R L, Park H and Lukin M D 2014 *Phys. Rev. Lett.* **113** 197601
[11] Ajoy A, Bissbort U, Lukin M D, Walsworth R L and Cappellaro P 2015 *Phys. Rev. X* **5** 011001
[12] Lovchinsky I *et al* 2016 *Science* **351** 836–41
[13] Mamin H J and Rugar D 2001 *Appl. Phys. Lett.* **79** 3358–60
[14] Rugar D, Budakian R, Mamin H and Chui B 2004 *Nature* **430** 329–32
[15] Degen C, Poggio M, Mamin H, Rettner C and Rugar D 2009 *Proc. Natl Acad. Sci.* **106** 1313–7
[16] Rose W, Haas H, Chen A Q, Jeon N, Lauhon L J, Cory D G and Budakian R 2018 *Phys. Rev. X* **8** 011030
[17] Poggio M and Degen C 2010 *Nanotechnology* **21** 342001
[18] Chernobrod B M and Berman G P 2005 *J. Appl. Phys.* **97** 014903
[19] Balasubramanian G *et al* 2008 *Nature* **455** 648–51
[20] Degen C, Poggio M, Mamin H and Rugar D 2008 *Phys. Rev. Lett.* **100** 137601
[21] Taylor J, Cappellaro P, Childress L, Jiang L and Budker D 2008 *Nat. Phys.* **4** 810
[22] Maletinsky P, Hong S, Grinolds M S, Hausmann B, Lukin M D, Walsworth R L, Loncar M and Yacoby A 2012 *Nat. Nanotechnol.* **7** 320
[23] Pelliccione M, Myers B A, Pascal L, Das A and Jayich A B 2014 *Phys. Rev. Appl.* **2** 054014
[24] Rondin L, Tetienne J P, Hingant T, Roch J F, Maletinsky P and Jacques V 2014 *Rep. Prog. Phys.* **77** 056503
[25] Rugar D, Mamin H, Sherwood M, Kim M, Rettner C, Ohno K and Awschalom D 2015 *Nat. Nanotechnol.* **10** 120–4
[26] Ofori-Okai B K, Pezzagna S, Chang K, Loretz M, Schirhagl R, Tao Y, Moores B A, Groot-Berning K, Meijer J and Degen C L 2012 *Phys. Rev. B* **86** 081406
[27] Rosskopf T, Dussaux A, Ohashi K, Loretz M, Schirhagl R, Watanabe H, Shikata S, Itoh K M and Degen C L 2014 *Phys. Rev. Lett.* **112** 147602
[28] Romach Y *et al* 2015 *Phys. Rev. Lett.* **114** 017601
[29] Kim M, Mamin H J, Sherwood M H, Ohno K, Awschalom D D and Rugar D 2015 *Phys. Rev. Lett.* **115** 087602
[30] Eichenfield M, Chan J, Camacho R M, Vahala K J and Painter O 2009 *Nature* **462** 78–82
[31] Schliesser A, Rivière R, Anetsberger G, Arcizet O and Kippenberg T J 2008 *Nat. Phys.* **4** 415–9
[32] Thompson J, Zwickl B, Jayich A, Marquardt F, Girvin S and Harris J 2008 *Nature* **452** 72–5
[33] Andrews R, Peterson R, Purdy T, Cicak K, Simmonds R, Regal C and Lehnert K 2014 *Nat. Phys.* **10** 321–6
[34] Regal C, Teufel J and Lehnert K 2008 *Nat. Phys.* **4** 555–60
[35] Rugar D and Grutter P 1991 *Phys. Rev. Lett.* **67** 699
[36] Chan J, Alegre T M, Safavi-Naeini A H, Hill J T, Krause A, Gröblacher S, Aspelmeyer M and Painter O 2011 *Nature* **478** 89–92
[37] Teufel J, Donner T, Li D, Harlow J, Allman M, Cicak K, Sirois A, Whittaker J D, Lehnert K and Simmonds R W 2011 *Nature* **475** 359–63
[38] Peterson R, Purdy T, Kampel N, Andrews R, Yu P L, Lehnert K and Regal C 2016 *Phys. Rev. Lett.* **116** 063601
[39] Yuan M, Cohen M A and Steele G A 2015 *Appl. Phys. Lett.* **107** 263501
[40] Nichol J M, Hemesath E R, Lauhon L J and Budakian R 2012 *Phys. Rev. B* **85** 054414
[41] Bargatin I and Roukes M 2003 *Phys. Rev. Lett.* **91** 138302
[42] Butler M C, Norton V A and Weitekamp D P 2010 *Phys. Rev. Lett.* **105** 177601
[43] Magusin P C and Veeman W S 2000 *J. Magn. Reson.* **143** 243–54
[44] Butler M C and Weitekamp D P 2011 *Phys. Rev. A* **84** 063407
[45] Wood C J, Borneman T W and Cory D G 2014 *Phys. Rev. Lett.* **112** 050501
[46] Bienfait A *et al* 2016 *Nature* **531** 74
[47] Haikka P, Kubo Y, Bienfait A, Bertet P and Mølmer K 2017 *Phys. Rev. A* **95** 022306
[48] Kleckner D, Pepper B, Jeffrey E, Sonin P, Thon S M and Bouwmeester D 2011 *Opt. Express* **19** 19708–16
[49] Norte R A, Moura J P and Gröblacher S 2016 *Phys. Rev. Lett.* **116** 147202
[50] Reinhardt C, Müller T, Bourassa A and Sankey J C 2016 *Phys. Rev. X* **6** 021001
[51] Arcizet O, Jacques V, Siria A, Poncharal P, Vincent P and Seidelin S 2011 *Nat. Phys.* **7** 879–83
[52] Kolkowitz S, Jayich A C B, Unterreithmeier Q P, Bennett S D, Rabl P, Harris J and Lukin M D 2012 *Science* **335** 1603–6
[53] Ovartchaiyapong P, Lee K W, Myers B A and Jayich A C B 2014 *Nat. Commun.* **5** 4429
[54] Blankenhorn M, Heintze E, Slota M, van Slageren J, Moores B A, Degen C L, Bogani L and Dressel M 2017 *Rev. Sci. Instrum.* **88** 094707
[55] Takahashi H, Okamoto T, Ishimura K, Hara S, Ohmichi E and Ohta H 2018 *Rev. Sci. Instrum.* **89** 083905

[56] Barg A, Tsaturyan Y, Belhage E, Nielsen W H, Møller C B and Schliesser A 2018 Measuring and imaging nanomechanical motion with laser light *Exploring the World with the Laser* (Berlin: Springer) pp 71–85

[57] Whitfield G and Redfield A G 1957 *Phys. Rev.* **106** 918–20

[58] Goldsborough J P, Mandel M and Pake G E 1960 *Phys. Rev. Lett.* **4** 13–5

[59] Schweiger A and Ernst R 1988 *J. Magn. Reson.* **77** 512–23

[60] Van Itterbeek A and Labro M 1964 *Physica* **30** 157–60

[61] Wago K, Züger O, Wegener J, Kendrick R, Yannoni C S and Rugar D 1997 *Rev. Sci. Instrum.* **68** 1823–6

[62] Rugar D, Yannoni C S and Sidles J A 1992 *Nature* **360** 563

[63] Poggio M, Degen C L, Rettner C T, Mamin H J and Rugar D 2007 *Appl. Phys. Lett.* **90** 263111

[64] Longenecker J G, Mamin H J, Senko A W, Chen L, Rettner C T, Rugar D and Marohn J A 2012 *ACS Nano* **6** 9637–45

[65] Poggio M, Degen C L, Mamin H J and Rugar D 2007 *Phys. Rev. Lett.* **99** 017201

[66] Purdy T P, Peterson R W and Regal C A 2013 *Science* **339** 801–4

[67] Rossi M, Mason D, Chen J, Tsaturyan Y and Schliesser A 2018 *Nature* **563** 53–8

[68] Flowers-Jacobs N E, Hoch S W, Sankey J C, Kashkanova A, Jayich A M, Deutsch C, Reichel J and Harris J G E 2012 *Appl. Phys. Lett.* **101** 221109

[69] Kuhn S, Wachter G, Wieser F F, Millen J, Schneider M, Schalko J, Schmid U, Trupke M and Arndt M 2017 *Appl. Phys. Lett.* **111** 253107

[70] Schliesser A, Anetsberger G, Riviére R, Arcizet O and Kippenberg T J 2008 *New J. Phys.* **10** 095015

[71] Mamin H, Rettner C, Sherwood M, Gao L and Rugar D 2012 *Appl. Phys. Lett.* **100** 013102

[72] Meenehan S M, Cohen J D, Gröblacher S, Hill J T, Safavi-Naeini A H, Aspelmeyer M and Painter O 2014 *Phys. Rev. A* **90** 011803